Title

Characterization of Complex Interactions at the Gas–Solid Interface with in Situ Spectroscopy: The Case of Nitrogen-Functionalized Carbon

Journal

The Journal of Physical Chemistry C, 123(14)

ISSN

1932-7447

Authors

Dzara, Michael J
Artyushkova, Kateryna
Shulda, Sarah
et al.

Publication Date

2019-04-11

DOI

10.1021/acs.jpcc.9b00487

Peer reviewed

Characterization of Complex Interactions at the Gas–Solid Interface with in Situ Spectroscopy: The Case of Nitrogen-Functionalized Carbon

Michael J. Dzara,[†] Kateryna Artyushkova,[‡,⊥] Sarah Shulda,[§] Matthew B. Strand,[†] Chilan Ngo,[†] Ethan J. Crumlin,[∥] Thomas Gennett,[†,§] and Svitlana Pylypenko*[,†]

[†]Department of Chemistry, Colorado School of Mines, 1012 14th Street, Golden, Colorado 80401, United States

[‡]Department of Chemical and Biological Engineering, Center for Micro-Engineered Materials (CMEM), University of New Mexico, Albuquerque, New Mexico 87131, United States

[§]National Renewable Energy Laboratory, 15013 Denver West Parkway, Golden, Colorado 80401, United States

[∥]Advanced Light Source, Lawrence Berkeley National Laboratory, 1 Cyclotron Road, Berkeley, California 94720, United States

ABSTRACT: Interactions at the gas–solid interface drive physicochemical processes in many energy and environmental applications; however, the challenges associated with characterization and development of these dynamic interactions in complex systems limit progress in developing effective materials. Therefore, structure–property–performance correlations greatly depend on the development of advanced techniques and analysis methods for the investigation of gas–solid interactions. In this work, adsorption behavior of O_2 and humidified O_2 on nitrogen-functionalized carbon (N–C) materials was investigated to provide a better understanding of the role of nitrogen species in the oxygen reduction reaction (ORR). N–C materials were produced by solvothermal synthesis and N-ion implantation, resulting in a set of materials with varied nitrogen amount and speciation in carbon matrices with different morphologies. Adsorption behavior of the N–C samples was characterized by in situ diffuse reflectance infrared Fourier-transform spectroscopy (DRIFTS) and ambient pressure X-ray photoelectron spectroscopy (AP-XPS) experiments. A new analysis method for the interpretation of AP-XPS data was developed, allowing both the determination of overall adsorption behavior of each N–C material and identification of which nitrogen species were responsible for adsorption. The complementary information provided by in situ DRIFTS and AP-XPS indicates that O_2 adsorption primarily takes place on either electron-rich nitrogen species like pyridine, hydrogenated nitrogen species, or graphitic nitrogen. Adsorption of O_2 and H_2O occurs competitively on solvothermally prepared N–Cs, whereas adsorption of H_2O and O_2 occurs at different sites on N-ion implanted N–Cs, highlighting the importance of tuning the composition of N–C materials to promote the most efficient ORR pathway.

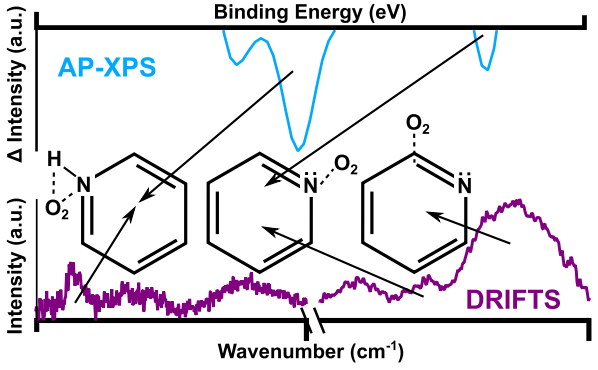

1. INTRODUCTION

The demand for advanced materials with controlled, unique properties is evergrowing as the complexity of novel devices and systems increases to meet societal challenges. Designing improved materials for applications such as heterogenous catalysis, gas storage in energy and environmental fields, adsorbents, and fuel cell and air battery electrode materials rely heavily on knowledge of surface properties, which largely depend on surface chemical speciation.[1−4] Interactions at the gas–solid interface are the foundation of many processes involved in these applications. However, these interfaces are often very complex, and the interactions are challenging to observe and interpret, further slowing progress in material development.[5−7]

Common techniques to quantify elemental speciation, correlate material properties to synthetic variables, and develop synthesis–property–performance relationships include but are not limited to: transmission and scanning transmission electron microscopies (TEM and STEM), energy-dispersive X-ray spectroscopy (EDS), Fourier-transform infrared spectroscopy, and X-ray photoelectron spectroscopy (XPS). Techniques such as these typically require high or ultrahigh vacuum (UHV), or are bulk measurements, making interactions between solids and gaseous species inaccessible under usual conditions. Utilizing in situ/in operando characterization through surface sensitive techniques like ambient

pressure XPS (AP-XPS) and diffuse reflectance infrared Fourier-transform spectroscopy (DRIFTS) enables the multimodal study of gas−solid interactions. AP-XPS and DRIFTS have been used to monitor surface changes, track adsorption behavior, and identify reactive intermediates in various material systems.[8−18] Complementary information obtained through AP-XPS and DRIFTS mitigates the drawbacks of the base techniques; the extreme surface sensitivity of DRIFTS balances the 1−10 nm information depth in AP-XPS, whereas the ability to quantify AP-XPS data and the breadth of different bonding types and chemical state information available from AP-XPS compensates for corresponding weaknesses in DRIFTS.[7,19] These are of particular value when investigating complex material systems and processes common to energy applications where corroborative multitechnique studies are needed.[20−22]

Carbon-based materials, from commonly used high surface area carbons such as carbon black to more novel nanostructures such as carbon nanotubes (CNTs) and graphene, are at the forefront of materials development for energy and environmental applications.[4,23−26] Nanostructured carbons are promising due to the breadth of carbon allotropes as well as the ability to tune the physical, chemical, and electronic properties through modifications of their composition, structure, and morphology. The applicability of carbon-based materials is expanded when considering carbon materials functionalized with various heteroatoms such as nitrogen, sulfur, phosphorous, and others.[27−29] In the case of nitrogen, which is very close in size to carbon and has one more electron, it is possible to control electronic properties without significant structural modification to the carbon matrix being functionalized.[29] Various methods that have been employed to incorporate nitrogen into carbon can generally be categorized into two groups: direct-incorporation (chemical synthesis of carbon structure including nitrogen containing precursors) and post-treatment (such as ammonia treatment or physical modification via implantation).[28−31] The inability of either synthetic route to produce single nitrogen functionalities and the diversity of functionalization approaches used across the literature results in the vast library of nitrogen species observed in the field. Such heterogeneity makes the characterization of the role of different nitrogen species present in nitrogen-functionalized-carbon (N−C) materials in various processes very challenging.[28,29,32]

A case of particular interest is the use of N−C materials in polymer electrolyte membrane fuel cells (PEMFCs), where they can act either as a support or an active component of the catalyst in the oxygen reduction reaction (ORR) at the cathode.[33−36] Replacing unmodified carbon supports with N−Cs has shown increased activity and durability of catalysts based on nanoparticles of platinum-group metals (PGMs) as well as PGM-free alternatives.[30,37,38] Both N−C and transition metal−N−C (M−N−C) materials have been studied as PGM-free catalysts, where certain nitrogen species are considered to be active for the ORR.[3,39] In the field of PEMFCs, the development of these PGM-free catalysts is crucial to meet the goal of drastic reduction in the amount of PGMs used in these devices.[2] Use of N−C materials may reduce reliance on PGMs by stabilizing PGM catalysts and/or as a component of PGM-free N−C and M−N−C catalysts, although both systems lack definitive understanding of the role that different nitrogen and nitrogen−metal species play in the ORR.[2,3,39] The literature suggests that multiple pathways are possible for the ORR on N−C and M−N−C-based electrocatalysts, featuring either a direct four-electron transfer or an indirect 2 × 2 electron transfer that may involve a hydrogen peroxide intermediate.[40,41] Since hydrogen peroxide is corrosive to PEMFC hardware, it is critical to understand which species are responsible for which pathway so that those promoting the desirable pathways can be maximized.[42] However, since the incorporation of nitrogen into high surface area carbons typically results in very heterogeneous materials with nitrogen present in a variety of functionalities and environments, it is difficult to isolate and assign activity/selectivity to the multitude of nitrogen species. This puzzle is made more complex in the case of generally more active M−N−C catalysts where both metal−nitrogen complexes and nitrogen species may contribute to the ORR. Therefore, it is key to understand the role of nitrogen species both for the goal of developing more active N−C and M−N−C catalysts and toward isolating the contributions of metal−nitrogen species in M−N−C catalysts.

An approach to elucidating the role of particular nitrogen species in the ORR is to develop model N−C materials with controlled surface features and to subsequently conduct fundamental mechanistic studies, often complemented by theoretical simulations. Typical model systems thus far have featured ordered carbons such as highly oriented pyrolytic graphite (HOPG), graphene, and carbon nanotubes (CNTs). Studies of HOPG materials where nitrogen was incorporated through N-ion implantation, while demonstrating a variety of nitrogen species, primarily indicated a correlation between pyridinic nitrogen and ORR activity.[38,41] Several experimental and density functional theory (DFT) studies on ORR mechanisms of N-doped graphene and N−CNTs have proposed that activity may be due to pyridinic nitrogen, graphitic nitrogen, or both species, with either the nitrogen atom or an adjacent carbon atom as active.[40,43−46] Additional work on N−CNTs suggests that different nitrogen species may support different steps of the ORR mechanism, indicating that the presence of multiple nitrogen moieties may be beneficial for ORR activity by enabling different reaction pathways.[47−49] Although studies of model N−C materials and theoretical work have enhanced the understanding of the role of specific nitrogen species in certain material systems, there is still no consensus on the respective contributions of each nitrogen species toward the possible steps of the ORR.

Of particular importance is the first step of the ORR that involves adsorption of O_2 to a potentially active site. Therefore, this work focuses on identifying the adsorption behavior of O_2 on N-doped carbons with different compositions and morphologies. To this end, a set of N−C materials with different surface properties was prepared by two methods: direct-incorporation (solvothermal synthesis resulting in size-controlled spheres) and post-treatment (N-ion implantation of carbon black and graphitic nanoplatelets (GnPs)).[38,50] All materials were characterized at UHV with STEM-EDS and laboratory source UHV-XPS to understand their composition and morphology. DRIFTS experiments in O_2 were conducted to confirm the adsorption of O_2 on the N−C samples and to complement the AP-XPS studies. AP-XPS studies were carried out at beamline 9.3.2 of the Advanced Light Source (ALS) synchrotron user facility at Lawrence Berkeley National Laboratory (LBNL), using lower photon energy (630 eV) at UHV and in O_2 with and without humidification.[51] Reduced photon energy provides more surface sensitive measurements

and permits subsequent analysis of subtle changes in the N 1s and O 1s spectra, enabling this work to shed light on the O_2 binding behavior of various nitrogen species.

2. EXPERIMENTAL SECTION

2.1. Solvothermal Synthesis. The preparation of nitrogen-functionalized carbon spheres ($N-C_{sph}$) was adapted from a previously reported solvothermal synthesis.[50] An aqueous alcohol solution was prepared from 320 mL of deionized H_2O (18.2 MΩ) and 128 mL of ethanol (Pharmco-Aaper, 200 proof absolute anhydrous) in in a 1 L high density polyethylene screwcap bottle while stirring at 300 rpm. Resorcinol (3.2 g, Sigma-Aldrich, >99%), 6.0 mL of ethylenediamine (Sigma-Aldrich, >99.5%), and 4.8 mL of formaldehyde (Alfa Aesar, 37 wt %) were added, while stirring continued for 24 h. Solvothermal conditions were then achieved by sealing the bottle with DuraFilm and heating at 100 °C for 24 h, after which the sealed bottle was cooled under running water. Polymerized spheres (PS) were isolated by centrifugation of the reaction mixture at 9000 rpm (9327 G) in a Marathon 22kbr centrifuge for 20 min, followed by aspiration of excess solution. The PS were then redispersed in ethanol, transferred into quartz boats, and air-dried at 70 °C for 12 h to drive off the ethanol. PS were then pulverized into a fine powder via mortar and pestle to ensure uniform treatment during pyrolyzation. Pyrolysis of PS was accomplished via thermal treatment at variable temperatures under N_2 flowing at 100 sccm. A quartz boat containing PS was heated at 2 °C/min to 350 °C, dwelled for 4 h, then heated at 5 °C/min to either 600, 700, or 900 °C, where it dwelled for 2 h before cooling to room temperature.

2.2. Nitrogen Implantation. Nitrogen functionalization of two commercially available carbons, a carbon black (Vulcan XC-72R, Cabot Corp.), and graphitic nanoplatelets (GnPs, Nanesa Inc.) was performed through ion implantation, as previously reported.[38,52] Approximately 500 mg of the carbon sample was placed in a rotating holder in the implantation chamber, which was evacuated to a base pressure of 5×10^{-6} Torr. The chamber was then refilled with pure N_2 to an operating pressure of $\sim 1 \times 10^{-3}$ Torr. A 3 cm direct current ion source (Veeco) was operated at a 13 mA beam current, 55 V discharge potential, and 100 V accelerator potential for 1 h while rotating the sample at 30 rpm to produce N-Vulcan or N-GnP.

2.3. STEM-EDS. STEM-EDS was conducted using an FEI Talos F200X operated at 200 kV. Samples were prepared by brushing Cu grids with holey C support films through the powders. Elemental EDS maps at various magnifications were acquired for up to 11 min per area, and data was both collected and processed by standard methods using Bruker ESPRIT software.

2.4. Quantitative XPS. Laboratory-based UHV-XPS was performed with a Kratos AXIS Nova photoelectron spectrometer using a monochromatic Al Kα source operating at 300 W (1486.6 eV). The operating pressure was 2×10^{-9} Torr. Survey and high-resolution spectra were acquired at pass energies of 160 and 20 eV, respectively. High-resolution spectra were recorded for the C 1s, O 1s, and N 1s core levels for all N−C materials. XPS data was processed using Casa XPS software. A linear background subtraction was used for the quantification of C 1s, O 1s, and N 1s regions. Elemental concentrations obtained from peak areas of high-resolution spectra of each element were used to evaluate surface composition. All spectra were charge referenced by adjusting the C 1s region to 284.5 eV, which is the average value obtained from the measurement of three spots on each sample mounted on conducting carbon tape.

2.5. DRIFTS. In situ DRIFTS was conducted using a Thermo Nicolet 4700 IR spectrometer fitted with a liquid-nitrogen-cooled MCT detector and Harrick Scientific Praying Mantis DRIFTS accessory with ZnSe windows. Spectra were collected as an accumulation of 1020 scans over a range of 4000−600 cm^{-1} at a resolution of 4 cm^{-1}. Each sample was heated to 150 °C at 10 °C/min and held for 1 h, then allowed to cool to 60 °C while maintaining high vacuum. A background spectrum was taken at 60 °C and used for subsequent spectra after oxygen introduction. The DRIFTS chamber was pressurized with approximately 1 Torr of oxygen, and IR data was collected under static oxygen pressure.

2.6. AP-XPS. Reduced photon energy UHV and AP-XPS was performed at beamline 9.3.2 at the ALS synchrotron user facility at LBNL.[51] Samples were dispersed in isopropyl alcohol and drop-cast onto conducting gas-diffusion-electrode carbon paper. All samples were first measured at ambient temperature under UHV ($<1 \times 10^{-8}$ Torr). High-resolution C 1s, O 1s, and N 1s spectra were collected with a photon energy of 630 eV and pass energy of 100 eV, excluding the N 1s, which had a pass energy of 50 eV. The same measurement settings were used to acquire data during in situ conditions (100 mTorr O_2 or 200 mTorr 1:1 O_2/H_2O dosed sequentially) at a temperature of 60 °C. In situ measurements were performed on the same area of analysis with the same focal distance as the initial UHV measurements. Deconvolution of N 1s and O 1s spectra was performed by a least squares method using a series of components with a 70% Gaussian, 30% Lorentzian line shape. For spectral subtraction, background-subtracted spectra were normalized by area before subtraction to account for differences in signal.

3. RESULTS AND DISCUSSION

3.1. Morphology and Elemental Distribution. A set of five N−C materials were prepared with systematically varied nitrogen amounts and speciation, introduced into the carbon either through chemical or physical methods. It is well documented that changing pyrolysis temperature can control both the amount and distribution of nitrogen functionalities incorporated in carbon-based materials.[28,29,50,53] Therefore, $N-C_{sph}$ synthesized here using a solvothermal treatment were pyrolyzed at 600, 700, and 900 °C. Physical routes such as nitrogen ion implantation are also known to produce a wide range of functionalities, with implantation parameters affecting the amount and speciation of incorporated nitrogen.[32,38,41,52] The distribution of functionalities in implanted samples greatly depends on not only the ion dosage but also the nature of each carbon material.[52] Two commercially available carbons were selected for this study, given their different shape, structure, and degree of graphiticity: Vulcan XC-72R and graphitic nanoplatelets. The various distributions of nitrogen environments in this set of samples should allow the comparison of adsorption behavior between N−C materials with different properties.

N−C materials were first characterized by STEM-EDS to better understand their differences in morphology, while also gaining insight into nitrogen content and spatial distribution. A collection of bright-field (BF) STEM images and corresponding elemental EDS maps for N and C (Figure 1) show the

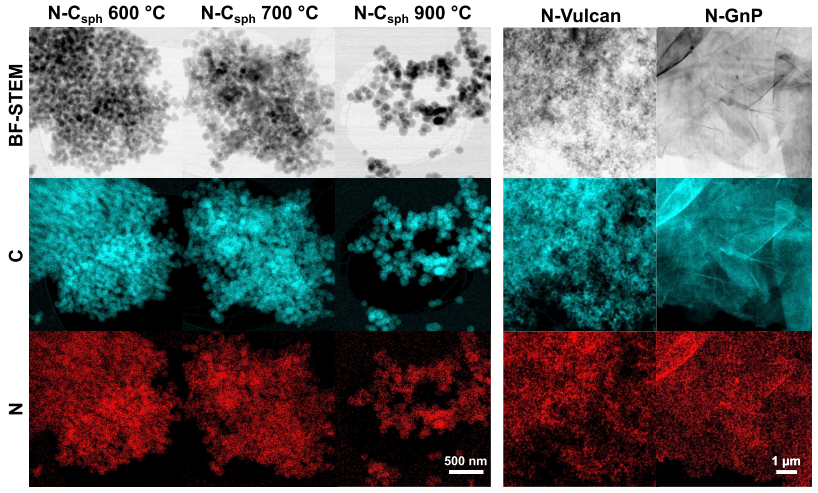

Figure 1. Representative BF-STEM images and EDS maps are shown, highlighting the morphology and elemental distribution of all N−C materials at lower magnification.

representative morphology and elemental distribution for each sample. Higher magnification images were taken in high angle annular dark-field (HAADF) STEM mode, showing the differences (or lack thereof) in morphology at different scales (Figure 2). The three N−C$_{sph}$ samples appear qualitatively

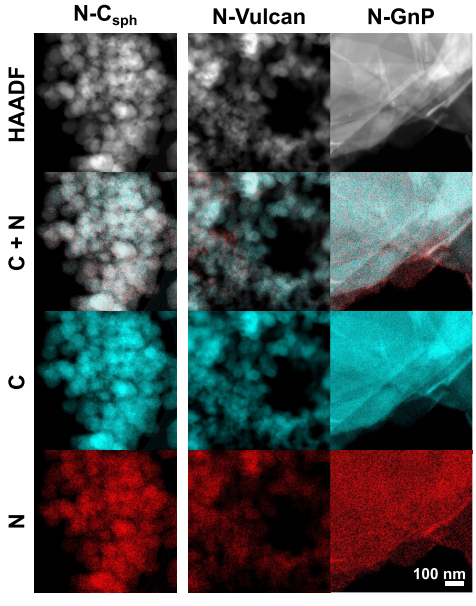

Figure 2. HAADF-STEM images and EDS maps (including C and N overlaid) are displayed, showing morphology and elemental distribution at higher magnification. N−C$_{sph}$ is represented by the sample pyrolyzed at 700 °C.

similar at both length scales, confirming that pyrolyzation temperature does not significantly impact particle size or nitrogen spatial distribution. As expected, N−C$_{sph}$ are spherical in shape and fairly uniform in size, around 100 nm in diameter. N-Vulcan has the typical features for this type of carbon: a variety of near-spherical particles fused together and more amorphous structures with features in the 20−50 nm range, which is shown more clearly at higher magnification (Figure 2). N-GnP shows the expected presence of many overlapping carbon sheets, with a random distribution of graphene sheet edges leading to regions of thicker or thinner nanoplatelets at the particle edges. All samples show a fairly even spatial distribution of nitrogen at lower magnification. Chemically modified samples (for which the 700 °C sample was selected as representative in Figure 2) show an even distribution of nitrogen, consistent with the incorporation of nitrogen throughout the bulk of N−C$_{sph}$. However, the physically modified samples show increased heterogeneity at the smaller scale. Since N-ion implantation is a line-of-sight technique, it is not likely that the entirety of the sample is accessible to be modified; it is thus not surprising to observe heterogeneity in the spatial distribution of nitrogen in the EDS maps, particularly with N-Vulcan. Heterogeneity can also be observed in the N-GnP sample at the edges of sheets which is likely due to the relative ease with which nitrogen can be implanted into the more defected edge sites.

Elemental concentrations were quantified from both EDS and lab-based UHV-XPS data (ST 1). EDS has an information depth on the order of 100 nm, whereas XPS quantifies the top 5−10 nm of material, enabling comparison of surface and bulk elemental concentration. Little to no difference in elemental concentration from EDS is seen amongst the chemically derived N−C$_{sph}$ materials, with 1.6−1.5 atomic % (at. %) oxygen and 1.9−1.8 at. % nitrogen present. From EDS, physically modified samples have less oxygen and nitrogen, with both samples having the same amount of oxygen (0.6 at. %) and slightly different amounts of nitrogen (0.6 at. % nitrogen in N-Vulcan vs 0.8 at. % in N-GnP). It is expected that the physically modified samples have less nitrogen in a bulk measurement as N-ion implantation only modifies the outermost layers of carbon, whereas chemical modification incorporates nitrogen throughout the material's surface and bulk. All samples have more oxygen and nitrogen present in the XPS quantification, indicating that these elements are enriched in the outermost few nanometers of the carbon structure. The oxygen concentration in chemically modified N−C materials decreases with increased pyrolyzation temperature, from 4.1 at. % at 600 °C to 3.6 at. % at 700 °C and finally to 3.1 at. % at 900 °C. The N−C$_{sph}$ pyrolyzed at 600 and 700 °C have a fairly similar nitrogen concentration, 3.1 and 3.0 at. % of nitrogen, respectively, but higher pyrolyzation temperature leads to loss of surface nitrogen (down to 2.0 at. %). Little difference exists between surface and bulk nitrogen concentrations (2.0 at. % from XPS vs 1.8 at. % from EDS) for

the 900 °C pyrolyzed sample, indicating that the decrease in total nitrogen with increased pyrolyzation temperature is primarily due to changing surface chemistry. Although the two physically modified samples were implanted under the same conditions, there is a significant difference: N-Vulcan shows relatively low amounts of heteroatoms, comparable to those observed in samples obtained from the thermochemical method (2.4 at. % of oxygen and 0.9 at. % of nitrogen), whereas N-GnP shows significantly higher amounts of heteroatoms (6.2 at. % of oxygen and 6.1 at. % of nitrogen) and introduced new nitrogen species that were not present on as-received samples.[52] This illustrates that the initial carbon structure is a key variable in physically modifying carbon with nitrogen—N-GnP has a very high relative amount of exposed edges that can be more easily implanted with nitrogen than the more continuous structure of Vulcan. The combination of STEM imaging, EDS mapping, and quantitative analysis of EDS and XPS spectra demonstrates that the spatial distribution and elemental concentration of nitrogen is varied, producing an interesting set of N−C materials for further study.

3.2. Distribution of Surface Nitrogen Species. Having characterized the amount and spatial distribution of nitrogen within the N−C materials, the next step is to better understand the types of nitrogen species present by examining the N 1s in greater detail. Properly deconvoluting the N 1s and assigning physical meaning to component peaks is particularly complex due to the abundance of possible nitrogen species in N−C materials and their relative proximity to each other in terms of binding energy (BE). Here, the full-width at half-maximum (FWHM) for each component was rigidly constrained to 1.0 eV, to show sensitivity toward subtle changes in the N 1s expected during the in situ experiments and to illuminate subtle compositional differences in samples. Fits of the N 1s in the literature are often comprised of only several components with FWHMs broader than 1.0 eV; however, it is impossible to assign such broader components to a single nitrogen species/environment. Even using numerous individual peaks with 1.0 eV FWHM, it remains a challenge to definitively assign a unique physical meaning to each peak, and therefore peaks are also grouped by the similarities in nitrogen bonding and electronic properties of the proposed species. For the initial fit of the N 1s, UHV-XPS collected at ALS with a photon energy of 630 eV was used (Figure 3). The spectrum of each material was fit with up to nine 1.0 eV peaks. Positions were rigidly constrained to a 0.2 eV BE range across all UHV data. Relative abundance, position, and FWHM of all components for each sample are reported in Table S2. Assigning physical species to the component peaks in the N 1s deconvolutions is based on a combination of previous work and a survey of the literature that encompasses theoretical calculations and experimental data on both reference materials and catalyst materials.[11,32,38,48,52,54−57] The lowest BE peak (397.6 eV) cannot be assigned to a single group and is attributed to nitrogen-rich species such as inorganic carbon nitrides, triazines, and multi-N-defect clusters. The component at 398.0−398.2 eV is assigned to the imine functional group and can encompass both aliphatic and aromatic imine species. The peak at 398.6−398.8 eV is attributed to pyridinic nitrogen. These three low BE components can be grouped and described as electron-rich nitrogen species, as low BE species are the most likely to have a higher electron density due to nitrogen lone pairs, the proximity of other nitrogen atoms in the carbon matrix, and resonant π bonding in aromatic rings. Species contributing to

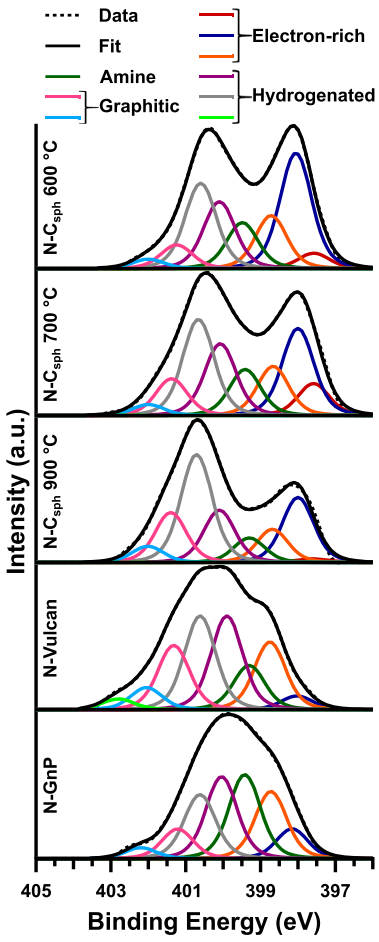

Figure 3. Deconvoluted N 1s spectra collected with synchrotron source energy (630 eV) at UHV and room temperature are shown for all N−C materials.

signal at 399.3−399.5 eV can be attributed to several functionalities, namely, amine and nitrile species. Previous work on N-Vulcan has concluded that this component is due to amine species, and it is unlikely that nitrile species will form in highly graphitic carbons.[52] Species located at 400.0−401.0 eV are commonly reported as a single peak and assigned to pyrrole; however, recent work combining DFT calculations and XPS measurement of reference materials has shown that signal in this region arises from both pyrrolic nitrogen and hydrogenated pyridinic nitrogen.[54] Therefore, the two components at 399.9−400.1 and 400.6−400.8 eV in our data are assigned to in-plane hydrogenated nitrogen species; when considered as one set of species, they contribute between a third and one-half of the total nitrogen species of each sample. For the remaining N 1s signal above 401 eV, three components were used to complete the fit of the N 1s. Graphitic nitrogen species have been assigned to a broad range of BE values in the literature, here two components are used to represent two possible regimes of graphitic nitrogen: graphitic nitrogen species in a more nitrogen-rich and/or less ordered environment (401.2−401.4) and graphitic N that can be viewed as a substitutional point defect in a well-ordered environment (402.0−402.2).[54] Protonated nitrogen (quaternary edge, in-plane protonated graphitic, or protonated edge pyridinic) can also contribute to these higher BE peaks. The final component ranges from 402.8 to 403.0 eV and is assigned to a mixture of oxidized organic nitrogen species such as oxidized pyridine and

hydrogenated nitrogen defects that are present at the edges of the graphitic carbon structure.[54,57]

From the analysis of N 1s spectra, we can see that there is a variation in nitrogen species from sample to sample. In general, both routes result in a large concentration of hydrogenated species, whereas the physical modification route produces larger amounts of pyridine and amine species, and direct incorporation via a chemical route results in larger amounts of imine species. For samples prepared via the chemical route, the relative proportions of major species can be tuned by changing the temperature. Imine, graphitic, and hydrogenated nitrogen species all increase with increased pyrolyzation temperature, whereas pyridine and amine species decrease at higher temperatures, corresponding to the loss of surface N observed in Table S1. The physically modified samples also show a preference for certain species, likely the result of differences in initial composition and structure of carbon. N-GnP has a higher proportion of imine and amine, whereas N-Vulcan has more hydrogenated and graphitic nitrogen, likely due to N-GnP having a larger proportion of edges where nitrogen can be more easily incorporated into the carbon structure. This analysis confirms that using both chemical and physical routes produces a diverse set of materials with different nitrogen speciations.

3.3. Oxygen Adsorption Studies by DRIFTS. The adsorption of oxygen is the first step in catalyzing the ORR; thus, to better understand the role of nitrogen, it is necessary to investigate the oxygen adsorption behavior of nitrogen species.[44] Initial study of O_2 adsorption was conducted with DRIFTS on a selected set of samples with the most different compositions and structures (N−C_{sph} 600 and 900 °C, N-Vulcan). A spectrum of the sample was collected under vacuum at 60 °C to serve as a background, prior to introducing approximately 1 Torr of oxygen. Performing the background correction in this fashion results in spectra with features due to the interactions between oxygen and the sample (Figure 4).

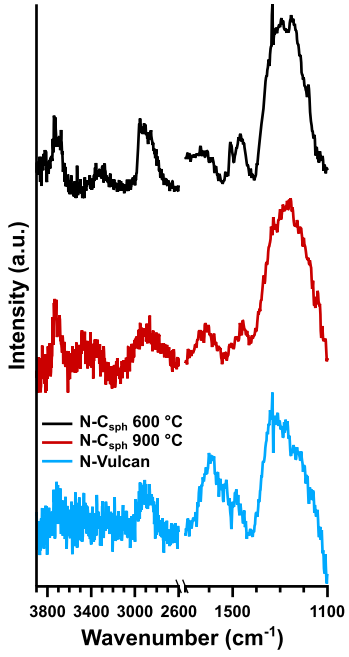

Figure 4. DRIFTS spectra show surface interactions due to exposure of N−C materials to 1 Torr of O_2 at 60 °C.

The three selected samples all have peaks aligning with the symmetric NO_2 stretch between 1320 and 1390 cm^{-1} and the asymmetric NO_2 stretch between 1485 and 1560 cm^{-1} indicating some degrees of oxygen adsorption to nitrogen sites in all samples. Spectra from each sample also contain evidence of carbon−oxygen interaction with strong IR absorption in the 1100−1300 cm^{-1} range, consistent with C−O stretching.[19,58] However, there are several differences in other spectral features that point to different adsorption processes on each sample.

Two broad lower energy hydroxyl stretches between 3200−3400 and 3400−3570 cm^{-1} are present primarily in N−C_{sph} samples and correspond to the O−H stretch of hydrogen-bonded hydroxyl groups.[19] Hydrogen-bonded hydroxyl O−H stretching character can be attributed to the adsorption of oxygen to hydrogenated nitrogen species, as it has previously been suggested that adsorption of this nature would result in interactions of oxygen with both the nitrogen and the hydrogen in a hydrogenated nitrogen species.[11,59] The N−C_{sph} materials pyrolyzed at 600 and 900 °C both have a strong and relatively sharp peak at approximately 3730 cm^{-1}, which correlates to a free hydroxyl O−H stretch, as does the peak at 3690 cm^{-1}.[60−62] This feature may be due to resonant effects of oxygen adsorption to carbon that induces oxygen−hydrogen interactions.

Although the N−C_{sph} samples both have strong O−H stretching features, the N-Vulcan sample shows more strong NO stretches at lower wavenumber, indicating that the adsorption to hydrogenated nitrogen is not the only process occurring. The broad feature at 2800−2900 cm^{-1} corresponding to alkane-like C−H stretching can shed light onto two other possible adsorption processes occurring: oxygen interaction with electron-rich nitrogen in an aromatic ring, such as pyrimidine or pyridine, or interaction with graphitic nitrogen species that both result in a loss of electron density at the nitrogen atom.[11,63] As the nitrogen atom is no longer donating as much electron density to the aromatic ring, it follows that there may be a loss of C═C π bonding and a subsequent increase in the alkane-like character due to resonant effects. All three samples show an increase in alkane character, indicating adsorption to either electron-rich nitrogen, graphitic nitrogen species, or graphitic carbon.

Adsorption to hydrogenated species occurs in all three samples measured with DRIFTS and is indicated by hydrogen-bonded hydroxyl O−H stretching. Electron-rich nitrogen species and graphitic nitrogen are characterized by an increase in alkane-like C−H stretching. It should be noted that all samples measured with DRIFTS show some degrees of carbon−oxygen interaction; this could be due to either direct adsorption to carbon species or weaker interactions with a neighboring carbon when oxygen adsorbs to a nitrogen species in an aromatic carbon structure. Through in situ DRIFTS analysis of oxygen adsorption in N-Vulcan and N−C_{sph} 600 and 900 °C samples, we have confirmed that adsorption of O_2 is occurring on chemically and physically derived N−Cs, indicating that both nitrogen and carbon species participate in the adsorption process, with notable variations stemming from differences in available nitrogen functionalities.

3.4. Oxygen and Water Adsorption Studies by AP-XPS. Adsorption behavior differences are further elucidated using AP-XPS at the ALS. In the interest of mimicking the operating conditions of a fuel cell, AP-XPS was performed on all N−C materials with a photon energy of 630 eV in 100

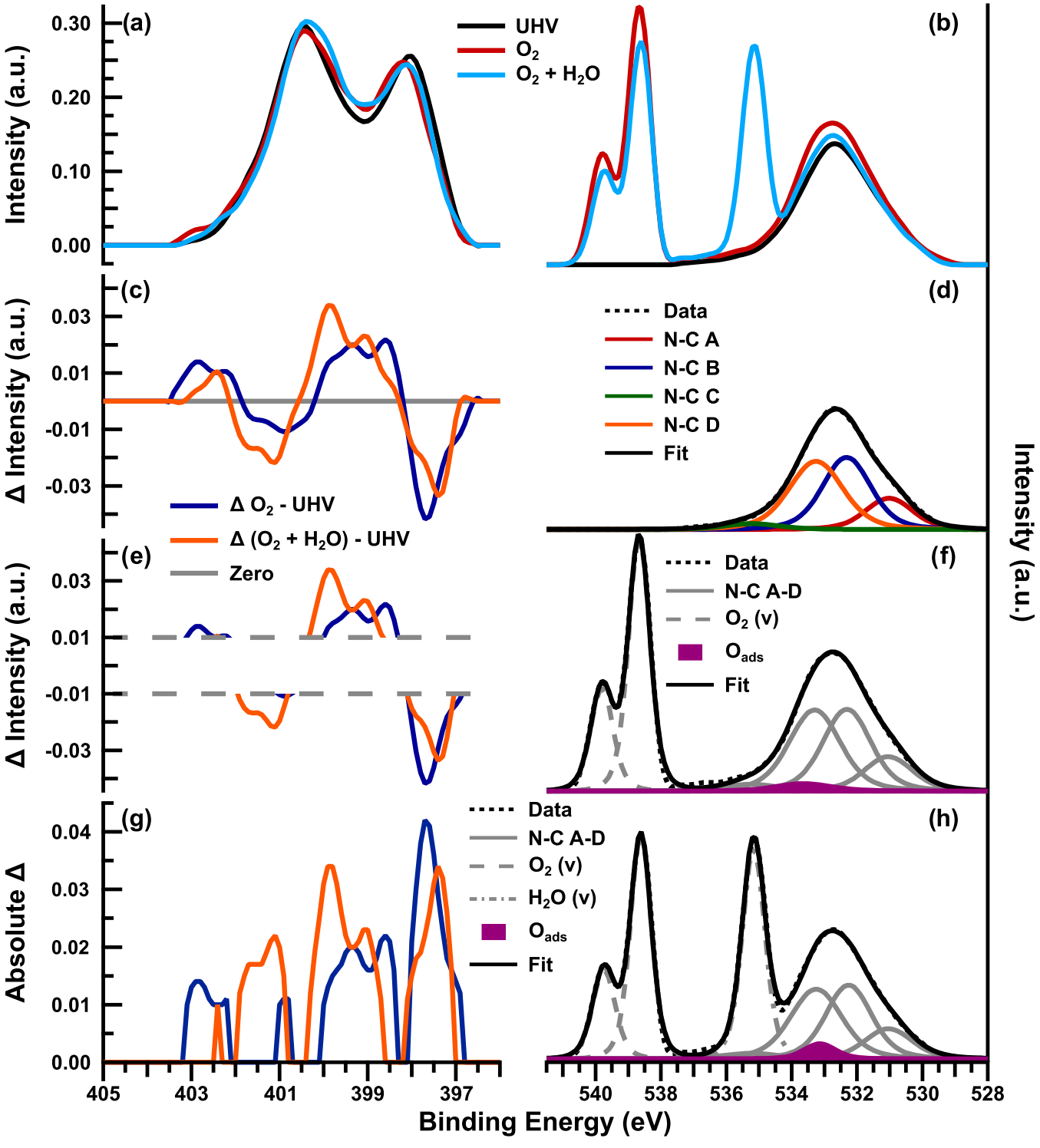

Figure 5. Overlaid data is shown for the N 1s (a) and the O 1s (b). To account for inactive and subsurface species, N 1s difference spectra are calculated (c), whereas ambient temperature UHV O 1s data is deconvoluted (d). A threshold (±0.01) was applied to the N 1s difference spectra to remove contributions from noise (e) and allow identification of adsorbing nitrogen species. Deconvoluted O 1s in 100 mTorr of O_2 at 60 °C is shown (f). The absolute value of the difference spectra was taken (g) to allow quantification of the total change in the N 1s. Deconvoluted O 1s in 100 mTorr of O_2 and 100 mTorr of H_2O at 60 °C is shown (h).

mTorr of O_2 at 60 °C, and then in 200 mTorr of approximately 1:1 O_2 and H_2O, also at 60 °C. These measurements are performed sequentially by adding water vapor to the oxygen that is already present. The N 1s has been fit for both the oxygen (Figure S1) and humidified oxygen (Figure S2) conditions, with the corresponding fitting parameters available in Tables S4 and S5. A similar strategy in peak deconvolution was applied as in Figure 3: FWHM values were set at 1.0 eV, whereas positions were set to the same value as used to fit the UHV data. This approach attempts to account for any changes in the N 1s by allowing

only one variable, the relative percentage of the components, to change in response to shifts in the data.

Several intricacies are associated with the analysis of such data. Even with the increased surface sensitivity of the reduced photon energy measurements, the fraction of data that comes from the true surface that adsorbs gaseous species is small and the covalent interactions between gas and nitrogen species are weak, resulting in very subtle changes in the XPS spectra. With the presence of different types of nitrogen species, a multitude of binding energy shifts can occur upon adsorption on these various sites. Oxygen bound directly to a nitrogen species that is bonded only to carbon, as in the case of pyridine, will draw electron density away from the nitrogen atom and result in a positive shift to higher BE.[11,63] However, in the case of hydrogenated nitrogen species, the interaction between the adsorbed gas and hydrogen atom results in an increase of electron density around the nitrogen atom and a subsequent shift to lower BE in the N 1s.[11,59] Therefore, on samples with hydrogenated and nonhydrogenated nitrogen species, it is likely that gas adsorption will result in competitive shifts as hydrogenated species move to lower BE and nonhydrogenated species move to higher BE. When fitting data, shifts would appear as changes in the relative amounts of components or changes in position. Allowing both position and relative percentage to change will result in a deconvolution that matches the in situ data, however allowing two variables to change will reduce the confidence with which spectral deconvolution changes can be assigned to physical processes. The fits (Figures S1 and S2) have position constrained; however, the quality of fit suffers and sensitivity to small shifts is lost, therefore a different approach to analysis must be employed.

An alternative data analysis methodology (Figure 5) was developed to overcome the above challenges. Interpretation of the N−C_{sph} sample pyrolyzed at 700 °C is shown as an example. Since our main goal is to identify the role of nitrogen species in oxygen adsorption, the N 1s and O 1s high-resolution spectra are examined. First, overlays of background-subtracted, area-normalized N 1s and O 1s data are shown. Changes in the spectral features of the N 1s (Figure 5a) are similar for the oxygen and humidified oxygen conditions, primarily impacting the region between 397 and 401 eV. If such changes in the N 1s are indeed due to O_2 adsorption, corresponding changes should also be present in the O 1s. The most intense peaks present in the O 1s (Figure 5b) are from the gas phase itself, as resolved in the doublet (538.7 and 539.8 eV) corresponding to O_2 gas and the single peak (535.2 eV) due to H_2O vapor. Now, it is necessary to isolate the changes due to gas−solid interactions. In the case of the N 1s, the difference spectra are calculated by subtracting the UHV data from spectrum collected at each atmosphere (Figure 5c). Changes up to ∼10% of the total normalized signal are observed. Difference spectra are not easily employed in the case of the O 1s due to the presence of the gas phase signal. Discounting the O_2 gas signal is simple due to its separation in BE from the O 1s signal attributed to the N−C structure; however, the peak due to water vapor overlaps that of the sample. In this case, a thorough curve fitting can be applied to identify adsorbed oxygen and water species. The initial O 1s region from the sample in UHV is fit by four components (Figure 5d), with contributions from different carbon−oxygen species. This allows both the unchanged oxygen species in the N−C solid and the gas phase peaks to be accounted for. Fits of the O 1s under UHV for all samples can be found in Figure S3, with the corresponding fitting parameters in Table S5. Now, both the solid adsorbate species and the adsorbed gaseous species can be identified. It is important to consider that some of the N 1s changes may come from instrumental noise. With this in mind, a threshold was applied to discount changes with a normalized intensity value of less than 0.01 au, approximately 3% of the max intensity of the N 1s (Figure 5e). This threshold value was validated by calculating the difference spectra of repeated UHV measurements conducted on the same area of analysis (Figure S4). Due to the nature of synchrotron experiments, there are additional challenges to face concerning the collection of a statistically significant amount of data to enable more robust error evaluation. In particular, there exists a trade-off between repeating measurements and characterizing a broad enough range of samples with varied properties to elucidate trends within a finite amount of experiment time. This strategy may eliminate some small changes due to physical processes; however, this is acceptable within the goal of identifying the main adsorbing species. In difference spectra, a negative peak should be due to species that are actively adsorbing O_2 and have decreased intensity due to a shift in BE induced by covalent interaction with an adsorbed gas species. Positive peaks are representative of a "destination" species, referring to the new BE of the nitrogen species covalently interacting with adsorbed gas. To better understand the adsorbed gas species, the fit used for the O 1s UHV data (i.e., peak positions, FWHMs, and area ratios amongst each other) is rigidly constrained and applied to the data acquired in the presence of oxygen (Figure 5f). After the peaks accounting for the gas phase O_2 are added, an additional loosely constrained peak is added to complete the curve fit. This peak accounts for any difference in the O 1s associated with adsorption on the N−C material. Here, a single broad peak with low intensity is required to complete the fit and is assigned to adsorbed O_2 (O_{ads}). By quantifying the percentage of the O 1s that is assigned to adsorbed gas relative to the total oxygen in the N−C material, differences in amount of gas adsorbed can be identified. As the amount of gas phase signal varies for each sample, contributions from the gas phase components are omitted when quantifying O_{ads}. Toward this goal, a similar parameter can be generated for the N 1s by taking the absolute values of the N 1s difference spectra after thresholding (Figure 5g), then integrating to represent the magnitude of the total change in the N 1s due to gas adsorption. This will allow the overall adsorption behavior of the N−C materials to be tracked, and the contributions of N and C in adsorption to be analyzed—absolute difference spectra for all materials are shown in Figure S5. To complete the analysis, the same fitting approach from the O 1s data in O_2 atmosphere is applied to the humidified O_2 atmosphere data (Figure 5h). The new O_{ads} peak has a greater intensity than that of the O_2 atmosphere case, indicating the adsorption of both H_2O and O_2. Analyzing AP-XPS data in this holistic fashion allows for analysis of correlations between changes in the N 1s and overall adsorption behavior of N−C materials.

With a thorough method to analyze changes in XPS data due to gas adsorption established, we next apply it to the data obtained on the entire material set to identify adsorbing N species in both O_2 and humidified O_2 environments. The changes in the N 1s are observed through the generation of difference spectra for each atmosphere (Figure 6). Only a small difference can be seen in the UHV and atmospheric data for

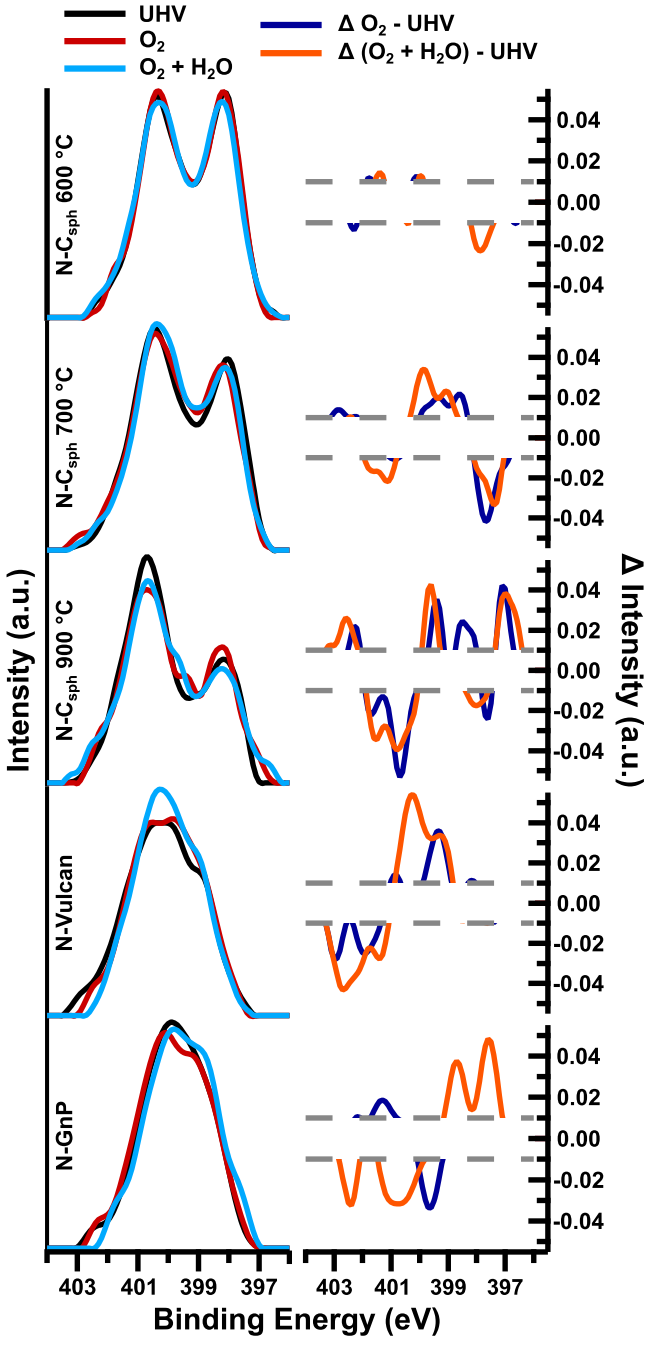

Figure 6. Overlaid N 1s spectra measured in UHV at ambient temperature, 100 mTorr O_2 at 60 °C, and 200 mTorr 1:1 O_2/H_2O at 60 °C are displayed for all samples, along with difference spectra calculated by subtracting the UHV spectrum from each in situ spectrum. Difference spectra are displayed with data below the threshold of instrumental noise removed.

the N−C_{sph} pyrolyzed at 600 °C, indicating that its nitrogen species are only somewhat active/available for O_2/H_2O adsorption. The remaining negative peaks after thresholding are present at positions that indicate O_2 binding to graphitic nitrogen (401−402 eV) and H_2O binding to electron-rich nitrogen (397.5−398.5 eV), supporting the conclusion from O_2 DRIFTS that the 600 °C sample has an adsorption process that increases alkane character due to resonant effects. More significant changes are seen in the N−C_{sph} samples pyrolyzed at higher temperatures. The 700 °C N−C_{sph} sample shows a primary negative peak at low BE for both O_2 and humidified O_2, indicating that the majority of its O_2 adsorption is taking place on electron-rich nitrogen species such as pyridine, pyrimidine, and N-clusters. With the addition of water vapor, a negative peak develops between 400 and 402 eV, indicating H_2O adsorption to hydrogenated and graphitic nitrogen species. For the 900 °C N−C_{sph} sample, negative peaks are present at positions that could indicate adsorption of O_2 to electron-rich nitrogen, graphitic nitrogen, and hydrogenated nitrogen, with the latter species producing the most prominent peak. This is in good agreement with what is observed with DRIFTS, as adsorption to graphitic and electron-rich nitrogen would cause the increase in alkane character observed, whereas adsorption to hydrogenated nitrogen explains the increase in O−H character that occurs. The difference spectra for O_2 and humidified O_2 conditions are very similar, indicating that O_2 and H_2O primarily adsorb at the same sites. N-Vulcan shows two negative peaks, at positions that indicate the adsorption to graphitic nitrogen, correlating to the adsorption behavior seen in DRIFTS, as the N-Vulcan sample displayed an increase in alkane character attributed to the adsorption of O_2 to graphitic nitrogen. The adsorption of H_2O in N-Vulcan occurs at the same sites as O_2 and with a more significant increase in magnitude than that of the N−C_{sph} samples. N-GnP shows the most variation in adsorption sites between the two atmospheres. In O_2, the only negative peak is ~399 eV, which suggests adsorption to amine species. In the case of humidified O_2, the main adsorption is taking place on hydrogenated nitrogen species. Among the chemically modified samples, most of the changes in the N 1s occur during O_2 adsorption, whereas the addition of H_2O increased the magnitude of some changes but did not significantly shift the peaks that are present in the difference spectra. With respect to the physically modified samples, there is less similarity between the peaks in the difference spectra at the two atmospheres. This indicates that the chemically modified samples primarily adsorb O_2 and H_2O at the same sites, whereas physically modified samples have sites that preferentially adsorb O_2 versus H_2O gaseous species.

To confirm that changes in the N 1s are due to gas adsorption and not other processes such as protonation, the changes in the O 1s were also evaluated by spectral deconvolution (Figure 7). Fitting parameters for each environment can be found in Tables S6 and S7. Components due to gas adsorption are slightly different for each sample, where the O_2 adsorption peak is at low BE (530.6 eV) for the N−C_{sph} sample pyrolyzed at 600 °C, whereas the O_{ads} component ranges from 533.6 to 534.4 eV for the remaining samples. Such behavior confirms that O_2 adsorption on different sites from sample to sample results in different perturbations in the O_2 electron density. There are slight changes in the BE of the O_{ads} component when H_2O vapor is introduced, with the largest shift occurring in N-GnP, from 534.4 to 532.7 eV, indicating that H_2O is likely adsorbing on a different site than O_2. All materials show an increase in the relative percentage of the O_{ads} component when H_2O vapor is introduced, confirming that some degrees of adsorption take place for both gases on all samples.

Overall adsorption trends for each gas environment can be examined from the above analysis of the O 1s and N 1s spectral regions by comparing the relative amount of the O 1s assigned to adsorbed gas species and the total change in the N 1s calculated by integrating the absolute area under the curve

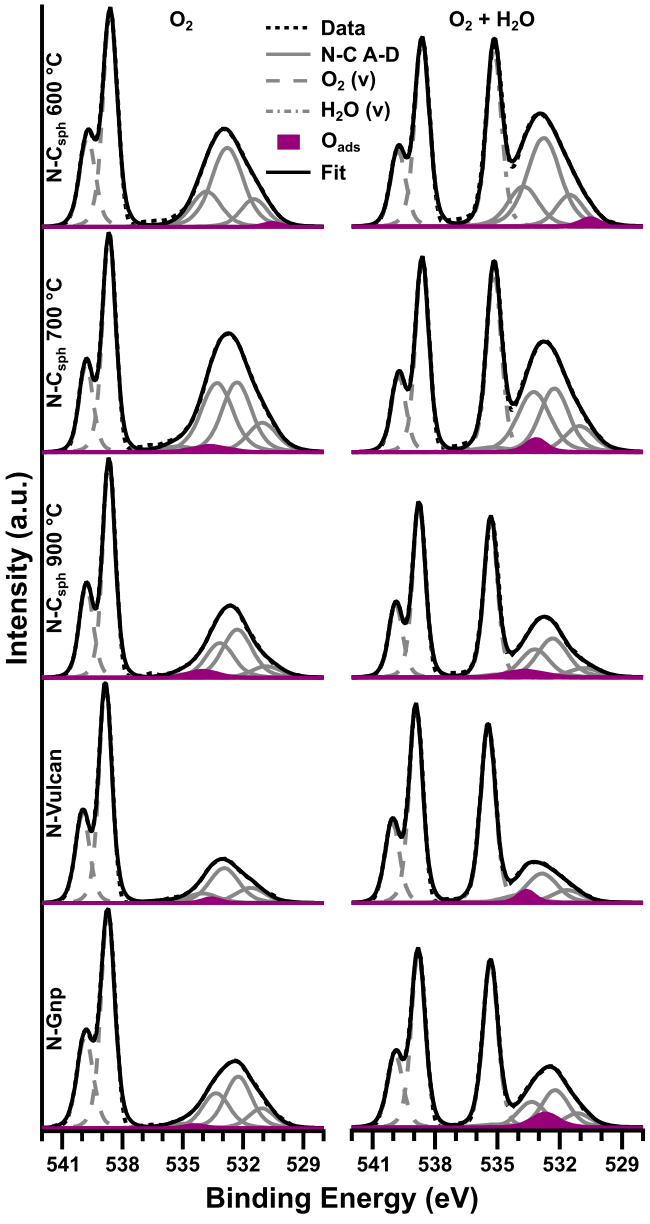

Figure 7. Deconvoluted O 1s spectra measured in 100 mTorr O_2 at 60 °C and 200 mTorr 1:1 O_2/H_2O at 60 °C are displayed for all samples.

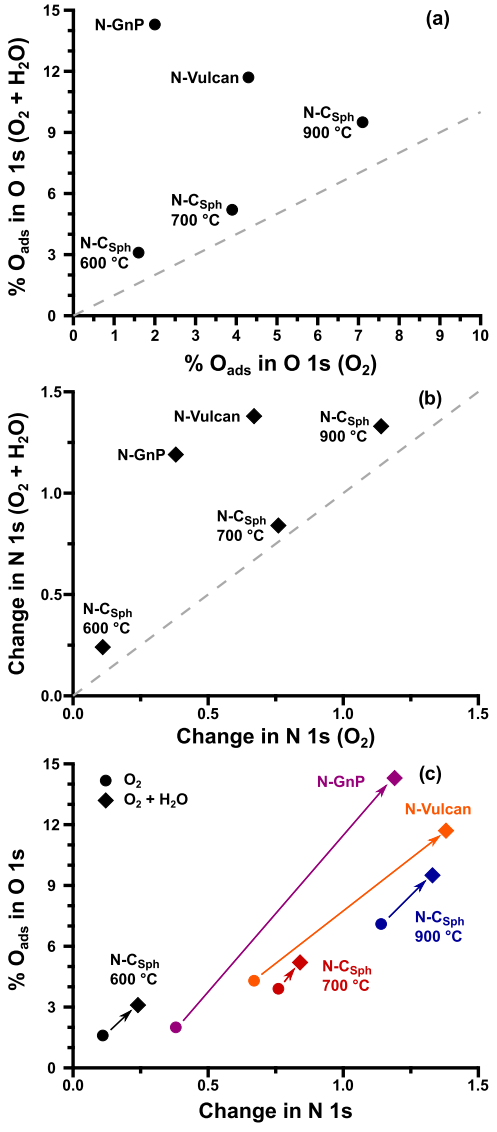

Figure 8. Trends in adsorption behavior are shown by comparing quantified relative changes in the N 1s and O 1s. Percentage of the O 1s attributed to adsorbed species is plotted for O_2 and H_2O atmospheres (a), along with the change in the N 1s from integrated absolute difference spectra (b). Both spectral regions are combined to show overall adsorption changes for each environment (c).

of the N 1s difference spectra (Figure 8). First, the contribution of the O_{ads} component due to O_2 adsorption is plotted on the x axis, whereas the O_{ads} component for humidified oxygen is plotted on the y axis (Figure 8a). The line $y = x$ is included, as a sample present on that line indicates that no further gas adsorption occurred when H_2O vapor was introduced following O_2 introduction. A sample above the $y = x$ line indicates that more gas is adsorbed when H_2O vapor is introduced following O_2 adsorption; all samples fall into this regime. The three chemically modified samples are only slightly above $y = x$, indicating much less adsorption of H_2O than O_2 vapor. Both N-Vulcan and N-GnP are well above the $y = x$ line, indicating that H_2O adsorption is still favorable despite the presence of adsorbed O_2; these observations suggest that O_2 and H_2O are adsorbing on different sites for the physically modified samples. The N 1s change is plotted for O_2 environment on the x axis and humidified O_2 on the y axis (Figure 8b), differing from Figure 8a in that it is specific to nitrogen only, hence any differences between the two plots should denote an interaction between gas and carbon, as that is the only other available species for gas adsorption. The chemically modified species and N-Vulcan show similar positions relative to the $y = x$ line to those in Figure 8a, indicating that the adsorption behavior characterized in the O 1s corresponds to nitrogen species. In contrast, N-GnP now has a value not as far above the $y = x$ when considering changes due to N only, suggesting that a portion of the O_2 adsorbed was due to carbon sites rather than nitrogen. The trends in oxygen adsorption behavior are summarized by showing the N 1s change (x axis) and the O 1s change (y axis) on the same plot for each atmosphere (Figure 8c). Changes in each of the chemically modified species are small and direct; thus, the majority of available adsorption sites are occupied by O_2 when H_2O is introduced and little adsorption of water occurs. For

the N-GnP sample, a significant increase that is much steeper than direct indicates that both H_2O and O_2 species are favorably adsorbed, likely due to the adsorption occurring at different active nitrogen and carbon species. N-Vulcan has a relationship between that of the chemically modified samples and N-GnP, significantly more H_2O is adsorbed than O_2; however, a greater proportion of this change is accompanied by changes in the N 1s than that of N-GnP. This suggests that N-Vulcan still has some adsorption of H_2O to carbon sites, but to a lesser extent than that of N-GnP. Considering that the N-ion implantation process can also create defects in the carbon structure other than the incorporation of nitrogen species, and that N-GnP is more impacted by the implantation process, it follows that the defected nature of these carbons would result in more adsorption to carbon species.

4. CONCLUSIONS

A set of five N−C materials was produced via two methods: a direct-incorporation, solvothermal treatment in which pyrolysis temperature was varied, and a post-treatment, N-ion implantation process in which the initial carbon structure was varied. STEM-EDS and UHV-XPS confirmed that these methods produced a variety of different nitrogen species and amounts incorporated into different carbon morphologies. In addition to thorough characterization of the samples in UHV to confirm the diverse set of nitrogen properties, several in situ studies were performed to better understand adsorption of O_2 and H_2O on N−C materials. Through analysis of difference spectra from both AP-XPS and DRIFTS, it was determined that each sample displayed adsorption of oxygen to different N−C functionalities. The N−C_{sph} sample pyrolyzed at 700 °C primarily adsorbed oxygen to electron-rich nitrogen species, whereas the 900 °C pyrolyzed N−C_{sph} sample adsorbed more to hydrogenated nitrogen species, with additional contributions from electron-rich nitrogen and graphitic nitrogen. Adsorption of oxygen to N-Vulcan took place on graphitic nitrogen and carbon species, whereas N-GnP adsorbed oxygen at aliphatic nitrogen species, possibly amine species. The 600 °C N−C_{sph} sample was the least active for adsorption of both gases. Physically modified samples were significantly more active for H_2O adsorption, likely due to a more defected carbon structure resulting from the N-ion implantation process. Since the participation of certain nitrogen species in the ORR has been linked to differences in selectivity of the possible ORR pathways, correlating such experiments with catalytic activity and moving toward in operando AP-XPS measurements in future studies may enable direct confirmation of which species are responsible for what steps of the ORR. This will be of particular value when applied to M−N−C catalysts, as this work provides a baseline study of adsorption behavior of nitrogen species that will aid in isolating the behavior of metal-containing sites from the behavior of N−C species. Overall, it is shown that multiple nitrogen species are able to adsorb oxygen and are therefore potentially active for the ORR, whereas a route is established for future AP-XPS analysis of subtle solid−gas interactions both in nitrogen containing materials and other relevant systems.

Tables of elemental composition from EDS and XPS; tables of XPS fitting parameters for all peak deconvolutions; peak deconvolutions of the N 1s during in situ measurements; peak deconvolution of the O 1s at UHV; duplicate N 1s spectra for thresholding; and the absolute value of thresholded N 1s difference spectra used for integration to determine the total change in N 1s difference spectra (PDF)

AUTHOR INFORMATION

Corresponding Author

*E-mail: spylypen@mines.edu.

ORCID

Kateryna Artyushkova: 0000-0002-2611-0422

Chilan Ngo: 0000-0003-4084-098X

Ethan J. Crumlin: 0000-0003-3132-190X

Svitlana Pylypenko: 0000-0001-7982-734X

Present Address

⊥Physical Electronics Inc.,18725 Lake Drive, East Chanhassen, Minnesota 55317, United States (K.A.).

Notes

The authors declare no competing financial interest.

ACKNOWLEDGMENTS

This work was supported by start-up funds from Colorado School of Mines and NSF Award #1800585—Probing Catalyst-Support Interactions via Experiment and Theory. This research used resources of the Advanced Light Source, which is a DOE Office of Science User Facility under contract no. DE-AC02-05CH11231. University of New Mexico acknowledges NSF Award # 1738386 RII Track-4: Operando Analysis of Fuel Cell Materials at Advanced Light Source. This work was authored in part by the National Renewable Energy Laboratory, operated by Alliance for Sustainable Energy, LLC, for the U.S. Department of Energy (DOE) under Contract No. DE-AC36-08GO28308. Funding provided by e.g., U.S. Department of Energy Office of Energy Efficiency and Renewable Energy Fuel Cell Technologies Office. The views expressed in this article do not necessarily represent the views of the DOE or the U.S. Government. The U.S. Government retains and the publisher, by accepting the article for publication, acknowledges that the U.S. Government retains a nonexclusive, paid-up, irrevocable, worldwide license to publish or reproduce the published form of this work, or allow others to do so, for U.S. Government purposes.

REFERENCES

(1) Cheng, F.; Chen, J. Metal-Air Batteries: From Oxygen Reduction Electrochemistry to Cathode Catalysts. *Chem. Soc. Rev.* **2012**, *41*, 2172−2192.

(2) Morozan, A.; Jousselme, B.; Palacin, S. Low-Platinum and Platinum-Free Catalysts for the Oxygen Reduction Reaction at Fuel Cell Cathodes. *Energy Environ. Sci.* **2011**, *4*, 1238.

(3) Dai, L.; Xue, Y.; Qu, L.; Choi, H.-J.; Baek, J.-B. Metal-Free Catalysts for Oxygen Reduction Reaction. *Chem. Rev.* **2015**, *115*, 4823−4892.

(4) Mauter, M. S.; Elimelech, M. Environmental Applications of Carbon-Based Nanomaterials. *Environ. Sci. Technol.* **2008**, *42*, 5843−5859.

(5) Park, S.-J.; Seo, M.-K. *Solid−Gas Interaction*; Academic Press, 2011; Vol. *18*.

(6) Nilsson, A.; Pettersson, L. G. M.; Norskov, J. *Chemical Bonding at Surfaces and Interfaces*; Elsevier Science, 2011.

(7) Bluhm, H.; Hävecker, M.; Knop-Gericke, A.; Kiskinova, M.; Schlögl, R.; Salmeron, M. In Situ X-Ray Photoelectron Spectroscopy Studies of Gas-Solid Interfaces at near-Ambient Conditions. *MRS Bull.* **2007**, *32*, 1022−1030.
(8) Casalongue, H. S.; Kaya, S.; Viswanathan, V.; Miller, D. J.; Friebel, D.; Hansen, H. A.; Nørskov, J. K.; Nilsson, A.; Ogasawara, H. Direct Observation of the Oxygenated Species during Oxygen Reduction on a Platinum Fuel Cell Cathode. *Nat. Commun.* **2013**, *4*, No. 2817.
(9) Ali-Löytty, H.; Louie, M. W.; Singh, M. R.; Li, L.; Casalongue, H. G. S.; Ogasawara, H.; Crumlin, E. J.; Liu, Z.; Bell, A. T.; Nilsson, A.; et al. Ambient-Pressure XPS Study of a Ni-Fe Electrocatalyst for the Oxygen Evolution Reaction. *J. Phys. Chem. C* **2016**, *120*, 2247−2253.
(10) Stoerzinger, K. A.; Favaro, M.; Ross, P. N.; Yano, J.; Liu, Z.; Hussain, Z.; Crumlin, E. J. Probing the Surface of Platinum during the Hydrogen Evolution Reaction in Alkaline Electrolyte. *J. Phys. Chem. B* **2018**, *122*, 864−870.
(11) Artyushkova, K.; Matanovic, I.; Halevi, B.; Atanassov, P. Oxygen Binding to Active Sites of Fe−N−C ORR Electrocatalysts Observed by Ambient-Pressure XPS. *J. Phys. Chem. C* **2017**, *121*, 2836−2843.
(12) Starr, D. E.; Liu, Z.; Hävecker, M.; Knop-Gericke, A.; Bluhm, H. Investigation of Solid/Vapor Interfaces Using Ambient Pressure X-Ray Photoelectron Spectroscopy. *Chem. Soc. Rev.* **2013**, *42*, 5833−5857.
(13) Yang, T. C.-K.; Wang, S.-F.; Tsai, S. H.-Y.; Lin, S.-Y. Intrinsic Photocatalytic Oxidation of the Dye Adsorbed on TiO_2 Photocatalysts by Diffuse Reflectance Infrared Fourier Transform Spectroscopy. *Appl. Catal., B* **2001**, *30*, 293−301.
(14) Jiang, M.; Koizumi, N.; Ozaki, T.; Yamada, M. Adsorption Properties of Cobalt and Cobalt-Manganese Catalysts Studied by in Situ Diffuse Reflectance FTIR Using CO and CO + H_2 as Probes. *Appl. Catal., A* **2001**, *209*, 59−70.
(15) Plaza, M. G.; Pevida, C.; Arenillas, A.; Rubiera, F.; Pis, J. J. CO_2 Capture by Adsorption with Nitrogen Enriched Carbons. *Fuel* **2007**, *86*, 2204−2212.
(16) von Deak, D.; Singh, D.; King, J. C.; Ozkan, U. S. Use of Carbon Monoxide and Cyanide to Probe the Active Sites on Nitrogen-Doped Carbon Catalysts for Oxygen Reduction. *Appl. Catal., B* **2012**, *113*−*114*, 126−133.
(17) Bezrodna, T.; Puchkovska, G.; Shimanovska, V.; Chashechnikova, I.; Khalyavka, T.; Baran, J. Pyridine-TiO_2 Surface Interaction as a Probe for Surface Active Centers Analysis. *Appl. Surf. Sci.* **2003**, *214*, 222−231.
(18) Crumlin, E. J.; Bluhm, H.; Liu, Z. In Situ Investigation of Electrochemical Devices Using Ambient Pressure Photoelectron Spectroscopy. *J. Electron Spectrosc. Relat. Phenom.* **2013**, *190*, 84−92.
(19) Coates, J. In *Interpretation of Infrared Spectra, A Practical Approach*; Meyers, R. A., Ed.; John Wiley & Sons Ltd., 2000.
(20) Teschner, D.; Wootsch, A.; Pozdnyakova-Tellinger, O.; Kröhnert, J.; Vass, E. M.; Hävecker, M.; Zafeiratos, S.; Schnörch, P.; Jentoft, P. C.; Knop-Gericke, A.; et al. Partial Pressure Dependent in Situ Spectroscopic Study on the Preferential CO Oxidation in Hydrogen (PROX) over Pt/Ceria Catalysts. *J. Catal.* **2007**, *249*, 318−327.
(21) Zhang, J.; Su, D. S.; Blume, R.; Schlögl, R.; Wang, R.; Yang, X.; Gajović, A. Surface Chemistry and Catalytic Reactivity of a Nanodiamond in the Steam-Free Dehydrogenation of Ethylbenzene. *Angew. Chem., Int. Ed.* **2010**, *49*, 8640−8644.
(22) Hwang, J.; Rao, R. R.; Katayama, Y.; Lee, D.; Wang, X. R.; Crumlin, E.; Venkatesan, T.; Lee, H. N.; Shao-Horn, Y. CO_2 Reactivity on Cobalt-Based Perovskites. *J. Phys. Chem. C* **2018**, *122*, 20391−20401.
(23) Dai, L.; Chang, D. W.; Baek, J.-B.; Lu, W. Carbon Nanomaterials for Advanced Energy Conversion and Storage. *Small* **2012**, *8*, 1130−1166.
(24) Liu, J.; Cui, L.; Losic, D. Graphene and Graphene Oxide as New Nanocarriers for Drug Delivery Applications. *Acta Biomater.* **2013**, *9*, 9243−9257.
(25) Li, B.; Cao, X.; Ong, H. G.; Cheah, J. W.; Zhou, X.; Yin, Z.; Li, H.; Wang, J.; Boey, F.; Huang, W.; et al. All-Carbon Electronic Devices Fabricated by Directly Grown Single-Walled Carbon Nanotubes on Reduced Graphene Oxide Electrodes. *Adv. Mater.* **2010**, *22*, 3058−3061.
(26) Titirici, M. M.; White, R. J.; Brun, N.; Budarin, V. L.; Su, D. S.; Del Monte, F.; Clark, J. H.; MacLachlan, M. J. Sustainable Carbon Materials. *Chem. Soc. Rev.* **2015**, *44*, 250−290.
(27) Paraknowitsch, J. P.; Thomas, A. Doping Carbons beyond Nitrogen: An Overview of Advanced Heteroatom Doped Carbons with Boron, Sulphur and Phosphorus for Energy Applications. *Energy Environ. Sci.* **2013**, *6*, 2839.
(28) Wang, H.; Maiyalagan, T.; Wang, X. Review on Recent Progress in Nitrogen-Doped Graphene: Synthesis, Characterization, and Its Potential Applications. *ACS Catal.* **2012**, *2*, 781−794.
(29) Wood, K. N.; O'Hayre, R.; Pylypenko, S. Recent Progress on Nitrogen/Carbon Structures Designed for Use in Energy and Sustainability Applications. *Energy Environ. Sci.* **2014**, *7*, 1212.
(30) Zhou, Y.; Neyerlin, K.; Olson, T. S.; Pylypenko, S.; Bult, J.; Dinh, H. N.; Gennett, T.; Shao, Z.; O'Hayre, R. Enhancement of Pt and Pt-Alloy Fuel Cell Catalyst Activity and Durability *via* Nitrogen-Modified Carbon Supports. *Energy Environ. Sci.* **2010**, *3*, 1437−1446.
(31) Ayala, P.; Arenal, R.; Rümmeli, M.; Rubio, A.; Pichler, T. The Doping of Carbon Nanotubes with Nitrogen and Their Potential Applications. *Carbon* **2010**, *48*, 575−586.
(32) Pylypenko, S.; Borisevich, A.; More, K. L.; Corpuz, A. R.; Holme, T.; Dameron, A. A.; Olson, T. S.; Dinh, H. N.; Gennett, T.; O'Hayre, R. Nitrogen: Unraveling the Secret to Stable Carbon-Supported Pt-Alloy Electrocatalysts. *Energy Environ. Sci.* **2013**, *6*, 2957−2964.
(33) Mamtani, K.; Ozkan, U. S. Heteroatom-Doped Carbon Nanostructures as Oxygen Reduction Reaction Catalysts in Acidic Media: An Overview. *Catal. Lett.* **2015**, *145*, 436−450.
(34) Shao, Y.; Sui, J.; Yin, G.; Gao, Y. Nitrogen-Doped Carbon Nanostructures and Their Composites as Catalytic Materials for Proton Exchange Membrane Fuel Cell. *Appl. Catal., B* **2008**, *79*, 89−99.
(35) Trogadas, P.; Fuller, T. F.; Strasser, P. Carbon as Catalyst and Support for Electrochemical Energy Conversion. *Carbon* **2014**, *75*, 5−42.
(36) Wang, D.-W.; Su, D. Heterogeneous Nanocarbon Materials for Oxygen Reduction Reaction. *Energy Environ. Sci.* **2014**, *7*, 576−591.
(37) Pylypenko, S.; Queen, A.; Olson, T. S.; Dameron, A.; Neill, K. O.; Neyerlin, K. C.; Pivovar, B.; Dinh, H. N.; Ginley, D. S.; Gennett, T.; et al. Tuning Carbon-Based Fuel Cell Catalyst Support Structures via Nitrogen Functionalization. II. Investigation of Durability of Pt-Ru Nanoparticles Supported on Highly Oriented Pyrolytic Graphite Model Catalyst Supports As a Function of Nitrogen Implantation. *J. Phys. Chem. C* **2011**, *115*, 13676−13684.
(38) Pylypenko, S.; Queen, A.; Olson, T. S.; Dameron, A.; Neill, K. O.; Neyerlin, K. C.; Pivovar, B.; Dinh, H. N.; Ginley, D. S.; Gennett, T.; et al. Tuning Carbon-Based Fuel Cell Catalyst Support Structures via Nitrogen Functionalization. I. Investigation of Structural and Compositional Modification of Highly Oriented Pyrolytic Graphite Model Catalyst Supports as a Function of Nitrogen Implantation D. *J. Phys. Chem. C* **2011**, *115*, 13667−13675.
(39) Masa, J.; Xia, W.; Muhler, M.; Schuhmann, W. On the Role of Metals in Nitrogen-Doped Carbon Electrocatalysts for Oxygen Reduction. *Angew. Chem., Int. Ed.* **2015**, *54*, 10102−10120.
(40) Zhang, L.; Xia, Z. Mechanisms of Oxygen Reduction Reaction on Nitrogen-Doped Graphene for Fuel Cells. *J. Phys. Chem. C* **2011**, *115*, 11170−11176.
(41) Guo, D.; Shibuya, R.; Akiba, C.; Saji, S.; Kondo, T.; Nakamura, J. Active Sites of Nitrogen-Doped Carbon Materials for Oxygen Reduction Reaction Clarified Using Model Catalysts. *Science* **2016**, *351*, 361−365.

(42) Borup, R.; Meyers, J.; Pivovar, B.; Kim, Y. S.; Mukundan, R.; Garland, N.; Myers, D.; Wilson, M.; Garzon, F.; Wood, D.; et al. Scientific Aspects of Polymer Electrolyte Fuel Cell Durability and Degradation. *Chem. Rev.* **2007**, *107*, 3904−3951.
(43) Yu, L.; Pan, X.; Cao, X.; Hu, P.; Bao, X. Oxygen Reduction Reaction Mechanism on Nitrogen-Doped Graphene: A Density Functional Theory Study. *J. Catal.* **2011**, *282*, 183−190.
(44) Kim, H.; Lee, K.; Woo, S. I.; Jung, Y. On the Mechanism of Enhanced Oxygen Reduction Reaction in Nitrogen-Doped Graphene Nanoribbons. *Phys. Chem. Chem. Phys.* **2011**, *13*, 17505.
(45) Xing, T.; Zheng, Y.; Li, L. H.; Cowie, B. C. C.; Gunzelmann, D.; Qiao, S. Z.; Huang, S.; Chen, Y. Observation of Active Sites for Oxygen Reduction Reaction on Nitrogen-Doped Multilayer Graphene. *ACS Nano* **2014**, *8*, 6856−6862.
(46) Gong, K.; Du, F.; Xia, Z.; Durstock, M.; Dai, L. Nitrogen-Doped Carbon Nanotube Arrays with High Electrocatalytic Activity for Oxygen Reduction. *Science* **2009**, *323*, 760−764.
(47) Wiggins-Camacho, J. D.; Stevenson, K. J. Mechanistic Discussion of the Oxygen Reduction Reaction at Nitrogen-Doped Carbon Nanotubes. *J. Phys. Chem. C* **2011**, *115*, 20002−20010.
(48) Sharifi, T.; Hu, G.; Jia, X.; Wågberg, T. Formation of Active Sites for Oxygen Reduction Reactions by Transformation of Nitrogen Functionalities in Nitrogen-Doped Carbon Nanotubes. *ACS Nano* **2012**, *6*, 8904−8912.
(49) Chen, Y.; Artyushkova, K.; Rojas-Carbonell, S.; Serov, A.; Matanovic, I.; Santoro, C.; Asset, T.; Atanassov, P. Inhibition of Surface Chemical Moieties by Tris(Hydroxymethyl)Aminomethane: A Key to Understanding Oxygen Reduction on Iron−Nitrogen−Carbon Catalysts. *ACS Appl. Energy Mater.* **2018**, *1*, 1942−1949.
(50) Wickramaratne, N. P.; Xu, J.; Wang, M.; Zhu, L.; Dai, L.; Jaroniec, M. Nitrogen Enriched Porous Carbon Spheres: Attractive Materials for Supercapacitor Electrodes and CO_2 Adsorption. *Chem. Mater.* **2014**, *26*, 2820−2828.
(51) Grass, M. E.; Karlsson, P. G.; Aksoy, F.; Lundqvist, M.; Wannberg, B.; Mun, B. S.; Hussain, Z.; Liu, Z. New Ambient Pressure Photoemission Endstation at Advanced Light Source Beamline 9.3.2. *Rev. Sci. Instrum.* **2010**, *81*, No. 053106.
(52) Wood, K. N.; Christensen, S. T.; Nordlund, D.; Dameron, A. A.; Ngo, C.; Dinh, H.; Gennett, T.; O'Hayre, R.; Pylypenko, S. Spectroscopic Investigation of Nitrogen-Functionalized Carbon Materials. *Surf. Interface Anal.* **2016**, *48*, 283−292.
(53) Wohlgemuth, S.-A.; White, R. J.; Willinger, M.-G.; Titirici, M.-M.; Antonietti, M. A One-Pot Hydrothermal Synthesis of Sulfur and Nitrogen Doped Carbon Aerogels with Enhanced Electrocatalytic Activity in the Oxygen Reduction Reaction. *Green Chem.* **2012**, *14*, 1515−1523.
(54) Matanovic, I.; Artyushkova, K.; Strand, M. B.; Dzara, M. J.; Pylypenko, S.; Atanassov, P. Core Level Shifts of Hydrogenated Pyridinic and Pyrrolic Nitrogen in the Nitrogen-Containing Graphene-Based Electrocatalysts: In-Plane vs Edge Defects. *J. Phys. Chem. C* **2016**, *120*, 29225−29232.
(55) Kabir, S.; Artyushkova, K.; Serov, A.; Kiefer, B.; Atanassov, P. Binding Energy Shifts for Nitrogen-Containing Graphene-Based Electrocatalysts - Experiments and DFT Calculations. *Surf. Interface Anal.* **2016**, *48*, 293−300.
(56) Artyushkova, K.; Kiefer, B.; Halevi, B.; Knop-Gericke, A.; Schlogl, R.; Atanassov, P. Density Functional Theory Calculations of XPS Binding Energy Shift for Nitrogen-Containing Graphene-like Structures. *Chem. Commun.* **2013**, *49*, 2539−2541.
(57) Chen, Y.; Matanovic, I.; Weiler, E.; Atanassov, P.; Artyushkova, K. Mechanism of Oxygen Reduction Reaction on Transition Metal-Nitrogen-Carbon Catalysts: Establishing the Role of Nitrogen-Containing Active Sites. *ACS Appl. Energy Mater.* **2018**, 5948.
(58) Stuart, B. H. *Infrared Spectroscopy: Fundamentals and Applications*; John Wiley & Sons Ltd., 2004.
(59) O'Shea, J. N.; Wang, C.; Luo, Y.; Schnadt, J.; Patthey, L.; Hillesheimer, H.; Krempasky, J.; Brühwiler, P. A.; Agren, H.; Mårtensson, N. Hydrogen-Bond Induced Surface Core-Level Shift in Isonicotinic Acid. *J. Phys. Chem. B* **2001**, *105*, 1917−1920.
(60) Mutch, G. A.; Shulda, S.; Mccue, A. J.; Menart, M. J.; Ciobanu, C. V.; Ngo, C.; Anderson, J. A.; Richards, R. M.; Vega-Maza, D. Carbon Capture by Metal Oxides: Unleashing the Potential of the (111) Facet. *J. Am. Chem. Soc.* **2018**, *140*, 4736−4742.
(61) Cadigan, C. A.; Corpuz, A. R.; Lin, F.; Caskey, C. M.; Finch, K. B. H.; Wang, X.; Richards, R. M. Nanoscale (111) Faceted Rock-Salt Metal Oxides in Catalysis. *Catal. Sci. Technol.* **2013**, *3*, 900−911.
(62) Fouad, N. E.; Thomasson, P.; Knözinger, H. IR Study of Adsorption and Reaction of Methylbutynol on the Surface of Pure and Modified MgO Catalysts: Probing the Catalyst Surface Basicity. *Appl. Catal., A* **2000**, *194−195*, 213−225.
(63) Stevens, J. S.; Byard, S. J.; Seaton, C. C.; Sadiq, G.; Davey, R. J.; Schroeder, S. L. M. Proton Transfer and Hydrogen Bonding in the Organic Solid State: A Combined XRD/XPS/ssNMR Study of 17 Organic Acid−base Complexes. *Phys. Chem. Chem. Phys.* **2014**, *16*, 1150−1160.